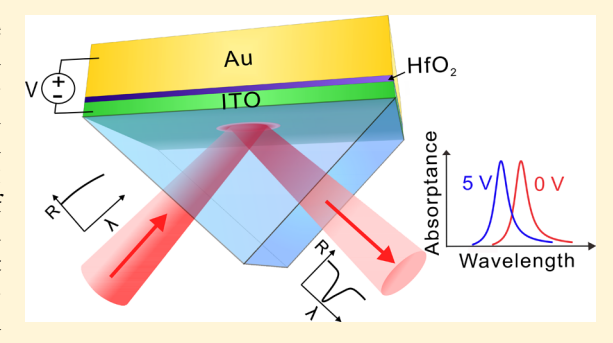


# Field-Effect Tunable and Broadband Epsilon-Near-Zero Perfect Absorbers with Deep Subwavelength Thickness

Aleksei Anopchenko,\*<sup>†,†</sup> Long Tao,<sup>†</sup> Catherine Arndt,<sup>†</sup> and Ho Wai Howard Lee\*,<sup>†,‡</sup>

Supporting Information

ABSTRACT: We report perfect light absorption due to the excitation of bound and radiative p-polarized optical modes in epsilon-near-zero (ENZ) conducting oxide nanolayers with thicknesses as thin as  $\lambda_{ENZ}/100$ . Perfect absorption in the wavelength range of 600 nm to 2  $\mu$ m may be achieved for unpatterned indium tin oxide (ITO) nanolayers with an electron density of  $5 \times 10^{20}$  to  $2 \times 10^{20}$ 10<sup>21</sup> cm<sup>-3</sup>. Multilayer stacks of ITO nanolayers with a gradient of electron densities and optimized thicknesses enable broadband perfect absorption. The postfabrication tuning, of the perfect absorption wavelength, of 32 nm is achieved in a metal-oxidesemiconductor (MOS) geometry with applied voltage of 5 V. Such ultrathin and tunable broadband perfect absorbers have many



potential applications in nonlinear flat ENZ optics, thermophotovoltaics, hot-electron generation in the ENZ regime, and other fields.

KEYWORDS: epsilon-near-zero, conducting oxides, perfect absorber, plasmonics, nanophotonics

ight harvesting and high-resolution optical technologies require optical coatings with strong light absorption. Perfect absorption (>99.9%), usually requires high optical losses and large thicknesses. Most optical dielectric materials, such as glasses, are transparent in the visible and infrared regions. Contrastingly, metals reflect light due to high optical losses. Because neither class of materials provides a satisfactory solution for strong optical absorption, there is significant interest in the development of new optical materials. Current materials include transparent conducting oxides, nano- and meta-materials, and 2D materials. 1-7 Interest in the development of new materials is spurred by technological demands for photonic integration, cost-efficient fabrication, and postfabrication tunability.8-15

Recent studies suggest that zero refractive index or epsilonnear-zero (ENZ) materials can be used to make perfect ultrathin film absorbers. 16-19 Ultrathin ENZ layers support radiative Berreman (above light line) and bound ENZ (below light line) modes. 20-24 Excitation of these modes leads to resonant light absorption. Degenerate transparent conducting oxides, for example, indium tin oxide (ITO), usually have high electron densities, N, ranging from 10<sup>19</sup> to 10<sup>21</sup> cm<sup>-3</sup>, resulting from the control of the deposition conditions. Specific electron densities allow an ENZ regime in the near-IR range. Therefore, conducting oxides are suitable ENZ materials for a multilayer broadband perfect absorber in the near-IR spectrum. In addition, by combining layers of a conducting oxide, a dielectric insulator, and a metal, a metal-oxide-semiconductor (MOS) field-effect structure can be formed to gate the conducting oxide ENZ materials. With field-effect modulation, plasmonic waveguide modulators with high modulation depth<sup>25</sup> and tunable conducting oxide metasurfaces or metamaterials<sup>26-2</sup> have been designed and demonstrated.

In this work, we present three aspects of ENZ perfect absorbers. First, we discuss the perfect absorption (PA) thickness dependence on ITO electron density and ENZ frequency. We calculate ITO nanolayer thicknesses required for achieving critical coupling to the Berreman and ENZ modes leading to PA, that is, >99.9%, and compare PA thicknesses for the two modes. Next, we present an ultrathin broadband perfect absorber for both modes composed of multilayer ITO stacks with gradient electron densities. Finally, we evaluate an optimal ITO thickness for PA field-effect tuning by investigating the relationships between ITO thickness, electron density, and incidence angle. We calculate postfabrication tunable PA through the formation of an electron accumulation/ depletion layer at the oxide-ITO interface in a MOS field-effect device with an ITO thickness <10 nm (Figure 1a).

# RESULTS AND DISCUSSION

Perfect Absorption in ENZ Nanolayers. We consider ppolarized (TM) light of wavelength  $\lambda$  incident at an angle  $\theta$ , in gadolinium gallium garnet (GGG) coupling prism, on an

Special Issue: Recent Developments and Applications of Plasmonics

Received: November 13, 2017 Published: April 23, 2018



<sup>&</sup>lt;sup>†</sup>Department of Physics, Baylor University, Waco, Texas 76798, United States

<sup>&</sup>lt;sup>‡</sup>The Institute for Quantum Science and Engineering, Texas A&M University, College Station, Texas 77843, United States

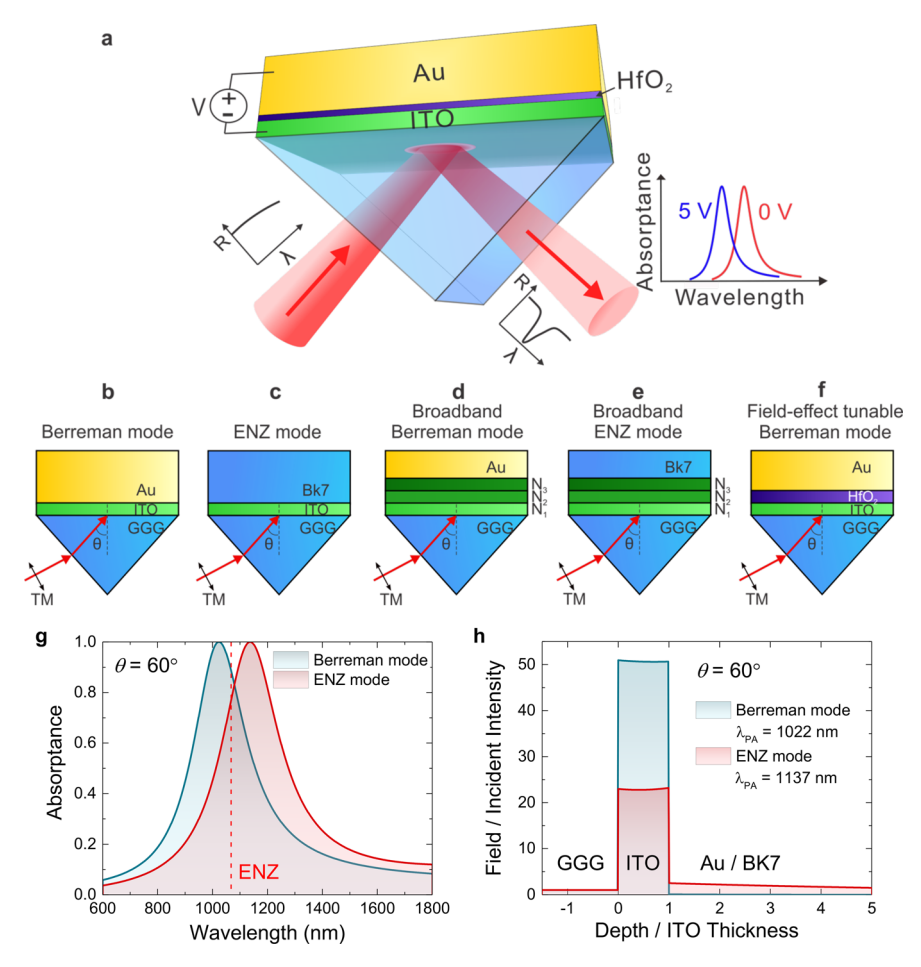


Figure 1. (a) Schematic of the field-effect tunable metal-oxide-semiconductor (MOS) ENZ perfect absorber. Schematic of the excitation of (b) the radiative Berreman mode and (c) the bound ENZ mode in the ultrathin ITO layers in the Kretschmann-Raether configuration; (d, e) broadband Berreman and ENZ modes in multilayered ITO configurations and (f) Berreman mode in the MOS configuration. The incidence medium is gadolinium gallium garnet (GGG). (g) Absorptance as a function of wavelength for an ITO layer with a thickness of 8.6 nm (Berreman mode) and 15.6 nm (ENZ mode) at an angle of incidence of 60°. The ITO thicknesses, incidence angle, and wavelength satisfy the perfect absorption condition of eq 1. Vertical dotted line shows an ENZ wavelength of 1067 nm. (h) Electric field intensity normalized to the incident intensity as a function of the depth normalized by the thickness of the ITO layer for both modes.

ultrathin ITO layer of thickness *t*. The incident light can excite the Berreman mode<sup>19–21,23</sup> if the external medium is metal, for example, gold (Figure 1b), or the ENZ mode<sup>24</sup> if the external medium is a dielectric with the refractive index smaller than the refractive index of the GGG prism, for example, BK7 glass (Figure 1c). The ENZ mode is excited in the Kretschmann-Raether configuration<sup>29</sup> with an incidence angle above the critical angle. The excitation of the TM modes in both structures leads to an enhanced electric field confined within the ITO layer and optical local density of states, resulting in strong light absorption. PA occurs when the wavelength, thickness, and angle values satisfy the condition for the critical coupling:<sup>22,23</sup>

$$\frac{2\pi t_{\rm PA}}{\lambda_{\rm PA}} = \left(\frac{{\rm Re}(\varepsilon_{\rm ITO})^2 + {\rm Im}(\varepsilon_{\rm ITO})^2}{n_{\rm GGG}^3 {\rm Im}(\varepsilon_{\rm ITO})}\right) \frac{1}{\sin \theta_{\rm PA} \tan \theta_{\rm PA}}$$
(1)

Here  $t_{\rm PA}$  is the ITO thickness, resulting in PA, satisfying eq 1,  $n_{\rm GGG}$  is the refractive index of the GGG prism (see Figure S1 in the Supporting Information for the refractive index dispersions of GGG, <sup>30</sup> BK7, and gold <sup>31</sup>). The frequency dependent complex electric permittivity of ITO,  $\varepsilon_{\rm ITO}$ , is described by the Drude model:  $\varepsilon_{\rm ITO} = \varepsilon_{\infty} - \frac{\omega_{\rm P}^2}{\omega^2 + i\omega\Gamma}$ , where  $\omega_{\rm P}^2 = \frac{Ne^2}{m^*\varepsilon_0}$  and

effective mass,  $\mu$  is the electron mobility,  $\varepsilon_0$  is the permittivity of free space,  $\varepsilon_{\infty}$  is the permittivity at infinite frequency,  $\omega_{\rm p}$  is the plasma frequency,  $\Gamma$  is the electron collision rate. In our absorptance calculations, we assume constant values for the electron effective mass ( $m^* = 0.28 m_0$ ), electron mobility ( $\mu =$ 31 cm<sup>2</sup>/(V·s)), and high frequency permittivity ( $\varepsilon_{\infty}$  = 3.6).<sup>32–34</sup> The ENZ frequency is defined as Re( $\varepsilon_{\rm ITO}$ ) = 0,  $\omega_{\rm ENZ}^2 = \frac{\omega_{\rm p}^2}{\varepsilon_{\infty}} - \Gamma^2$ . Figure 1g shows an example of PA at a wavelength of 1022 nm for the Berreman mode at an incidence angle of 60° on an ITO layer (blue curve). An electric field intensity enhancement of 50 (Figure 1h) is observed at the PA wavelength in the ITO layer with a thickness of 8.6 nm. Similarly, the ENZ mode (red curve) exhibits PA at a wavelength of 1137 nm and electric field intensity enhancement of 25 in a 15.6 nm thick ITO layer. For the absorptance and electric field intensity calculations see Methods. In the previous examples, the electron density of the ITO nanolayer is  $N = 1 \times$  $10^{21}$  cm<sup>-3</sup>, corresponding to an ENZ wavelength of  $\lambda_{ENZ}$  = 1067 nm. The PA wavelength of the ITO nanolayer may be varied within the near-IR range through the manipulation of the ITO electron density (see Figure S2 for electron densities of N

 $\Gamma = \frac{e}{m^* \mu}$ . Here e is the elementary charge,  $m^*$  is the electron

= 5  $\times$  10<sup>20</sup> cm<sup>-3</sup> and N = 2  $\times$  10<sup>21</sup> cm<sup>-3</sup>). The absorptance peak has the Lorentzian shape: <sup>17</sup>

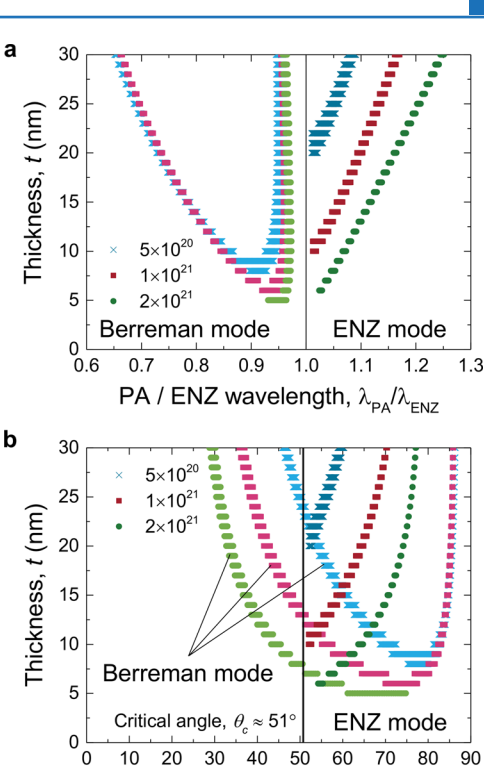
$$A(\omega) = \frac{4\gamma^2}{\left(\omega - \omega_{\rm PA}\right)^2 + 4\gamma^2} \tag{2}$$

Here  $\omega_{\rm PA}$  is the PA frequency and  $2\gamma \approx \varepsilon_{\infty}\Gamma$  is the full width at half-maximum (fwhm) of the absorptance peak. The fwhm does not depend on the electron density in the frequency/energy domain. Rather fwhm decreases when the electron density increases in the wavelength domain, that is, fwhm  $\propto 1/N$  (see Figure S2).

Equation 1 does not include explicit information about the optical properties of the external medium. Therefore, the PA condition implied by eq 1 are the same for both Berreman and ENZ modes. In order to determine the minimum ITO thickness required to achieve PA and to elucidate the obscured angular and wavelength dependence of the PA thickness in eq 1, we numerically calculate the PA thicknesses for both the Berreman and ENZ modes. Our numerical results show good agreement with eq 1 (Figure S3).

Despite the simplicity implied by eq 1, the PA conditions for two modes are distinctly different. Excitation of the Berreman mode in the ITO layer of a fixed thickness leads to PA at two different angles (wavelengths): one at small incident angles (PA wavelength is only slightly shorter than the ENZ wavelength) and another at incident angles >80° (shorter wavelengths). This observation is in agreement with prior work.<sup>22</sup> At small incident angles, the PA wavelength shows minor dependence on the ITO layer thickness (Figure 2a). In contrast to the Berreman mode, the ENZ mode exhibits a PA wavelength longer than the ENZ wavelength ( $\lambda_{PA}/\lambda_{ENZ} > 1$ ) and shows a strong dependence on ITO layer thickness (Figure 2a). Excitation of the ENZ mode results in resonant light absorption above the critical angle (Figure 2b). Our numerical results show a minimum ITO layer thickness below which PA is not obtainable for either mode. PA is achievable in deep subwavelength ITO nanolayers (<10 nm) for both Berreman and ENZ modes, for all numerically considered electron densities, as shown in Figure 2. It should be noted that high conductivity ultrasmooth ITO nanolayers with thicknesses of <10 nm might be difficult to fabricate by conventional techniques, requiring special fabrication processes and postfabrication treatments. However, our study is not limited to ITO and conducting oxides. Other ENZ materials, such as TiN, which have been shown experimentally in subten nanometer scale (<10 nm) with high film quality,<sup>35</sup> may be utilized.

An increase in the electron densities of the ITO layers results in thinner PA thicknesses. The PA thickness,  $\sim \lambda_{\rm ENZ}/100$ , may be as thin as 5 nm for an electron density of  $2 \times 10^{21}$  cm<sup>-3</sup> (cf.  $\lambda_{\rm PA} \approx \lambda_{\rm ENZ} = 752$  nm). The PA thicknesses are similar for the ENZ mode at the critical angle of ≈51° and the Berreman mode. In a range of incident angles (51° <  $\theta$  < 80°), PA thickness for the Berreman mode is smaller than that of the ENZ mode (Figure 2b). For all electron densities under our study, the Berreman mode requires thinner layers than those of the ENZ mode. The PA thickness difference for the two modes is more pronounced at lower electron densities (Figure 2c). As the electron density increases, PA thickness decrease more rapidly than the ENZ wavelength. The ENZ wavelength scales as  $\lambda_{\rm ENZ} \propto \frac{1}{\sqrt{N}}$ , while the PA thickness scales as  $t_{\rm PA} \propto \frac{1}{N^{\alpha}}$ , where the exponent  $\alpha \approx 1$  for the ENZ mode. The exponent  $\alpha$  $\approx$  1 may be inferred from eq 1 by using Re( $\varepsilon_{\text{ITO}}$ ) = 0 and



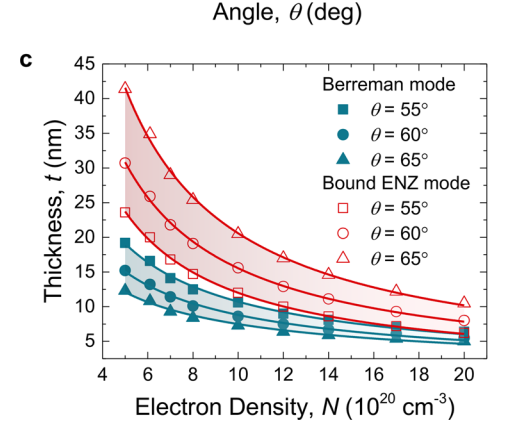
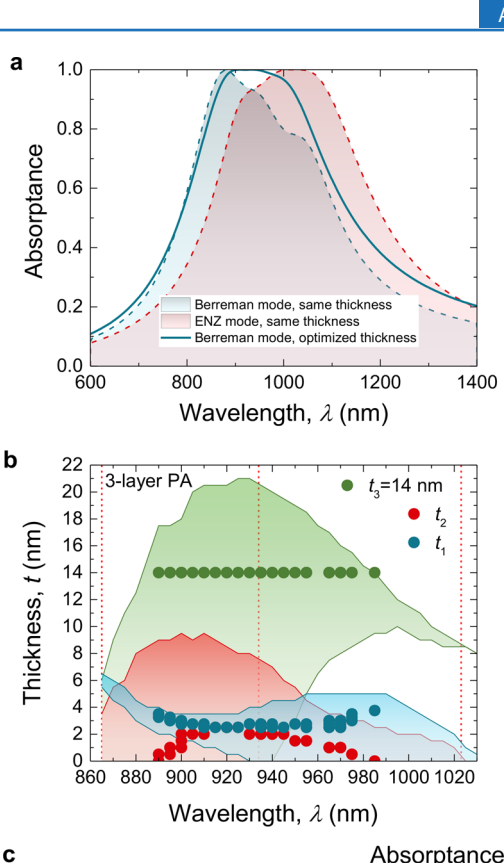


Figure 2. Relationships between (a) perfect absorption (PA) wavelength and PA thickness and (b) PA angle and PA thickness for the ENZ and Berreman modes. The relationships are computed for three ITO films with electron densities of 5  $\times$   $10^{20}$  cm<sup>-3</sup>,  $1 \times 10^{21}$ cm $^{-3}$ , and 2 × 10 $^{21}$  cm $^{-3}$  with corresponding ENZ wavelengths of 1519, 1067, and 752 nm, respectively. The PA wavelength is normalized to the corresponding ENZ wavelengths. Vertical lines show (a) the ENZ wavelength and (b) the critical angle at the ENZ wavelength  $\theta_c \approx 51^{\circ}$  (ENZ mode only; the critical angle is approximately the same for the three films). The relationships for both modes described by eq 1 exhibit good agreement with the numerical results (Figure S3). (c) Electron density dependence of the ITO thickness satisfying the PA condition of eq 1 for both Berreman and bound ENZ modes at three angles of incidence. The dots are the numerical results and the lines are linear regressions of  $t_{\rm ITO} \propto 1/N^{\alpha}$ , where  $\alpha \approx 1$ .

 ${\rm Im}(\varepsilon_{\rm ITO})=\frac{\varepsilon_{\infty}\Gamma}{\omega_{\rm ENZ}}$  in eq 1 and assuming  $\lambda_{\rm PA}\approx\lambda_{\rm ENZ}$ . For the Berreman mode,  $\alpha$  decreases from 0.83  $\pm$  0.02 to 0.69  $\pm$  0.03 as the incident angle increases from 55° to 65° (Figure 2c). The numerical relationships between ITO thickness, electron density, and incident angle of the single ultrathin ITO layer

enable development of perfect absorbers with nanoscale thicknesses.

Broadband Perfect Absorption in ENZ Multilayers. As shown previously, a single ITO layer at any incidence angle exhibits PA at a single wavelength despite the large fwhm of the absorption peak at low electron densities (fwhm  $\propto 1/N$ ). It is possible to create an absorber with a larger PA band by stacking ITO nanolayers with different electron densities 17,36 (Figure 1d,e). The PA bandwidth depends on the PA wavelengths of individual ITO layers, the number of ITO layers, and corresponding ITO layer thicknesses. An example of the broadband perfect absorber composed of three ITO nanolayers, all of the same thickness, is shown in Figure 3a for both the Berreman and the ENZ configurations. We consider a 3-layer ITO stack (Figure 1d, e) with electron densities  $N_1 = 1.4 \times 10^{-1}$  $10^{21}~\rm cm^{-3}$  (bottom layer),  $N_2=1.2\times 10^{21}~\rm cm^{-3}$  (middle layer), and  $N_3=1.0\times 10^{21}~\rm cm^{-3}$  (top layer). Each ITO layer's thickness is  $t_i = 4$  nm (Berreman mode) or  $t_i = 6$  nm (ENZ mode), where i is the ITO nanolayer index (i = 1, 2, and 3). The thicknesses are chosen to optimize the absorptance band at an incidence angle of 60°. Although the three-layer absorbers exhibit absorptance bands with large fwhm's, the bandwidth of PA (>99.9%) is negligible, that is, <4 nm (Figure 3a). A significant increase in the PA bandwidth for the ENZ mode is obtained by decreasing the incidence angle from 60° to 53°, that is, closer to the critical angle of 51° (Figures 3a and S4). As we show in Figure 3a, the ENZ mode has a PA bandwidth of 40 nm at the incidence angle of 53° (cf. the bandwidth of <4 nm for the Berreman configuration at the incidence angle of  $60^{\circ}$ ). Contrastingly, the PA bandwidth of the three-layer absorber for the Berreman mode does not increase when changing the incidence angle (Figure S4). Therefore, the ITO layer thicknesses must be optimized. We illustrate a thickness optimized broadband perfect absorber designed for the Berreman configuration in Figure 3b,c. In contrast to a single ITO layer, there are certain PA thickness domains for each ITO nanolayer in the three-layer stack (Figure S5). The boundaries of the domains are determined by the thickness-wavelength relationships of one pair of ITO nanolayers forming the threelayer stack, that is, with the third ITO nanolayer thickness set to zero (Figure S5). If the thickness of one ITO layer (e.g.,  $N_3$  =  $1.0 \times 10^{21} \text{ cm}^{-3}$ ) is fixed at a constant nonzero value, for example,  $t_3 = 14$  nm, then the two other layers of the threelayer perfect absorber will have the thickness-wavelength relationships shown in Figure 3b (solid circles). The domain's wide range of thicknesses leading to PA allow for the optimization of the PA bandwidth. The PA wavelength bandwidth of the three-layer absorber appears as a common wavelength range (ca. 900-945 nm) shared by the thicknesses  $t_1 = t_2 = 2.5$  nm and  $t_3 = 14$  nm from the thickness domains (Figure 3b). The PA bandwidth of 45 nm and total optimized multilayer thickness of 19 nm for the Berreman configuration are similar to the PA bandwidth of 40 nm and total thickness of 18 nm for the ENZ configuration (Figure 3a). Absorbers with more than 90% of absorption and a bandwidth of 170 nm (Berreman mode) and 190 nm (ENZ mode) are also achieved. Furthermore, formation of the absorptance band may be clearly observed over broad incidence angle and wavelength ranges. The absorptance of the optimized three-layer absorber as a function of the incident angle and wavelength is shown in Figure 3c. The broadband absorption (>90%) is obtained in a wavelength range of about 870-1050 nm and an incidence angle range of about 50-70° (Figure 3c). In principle, a



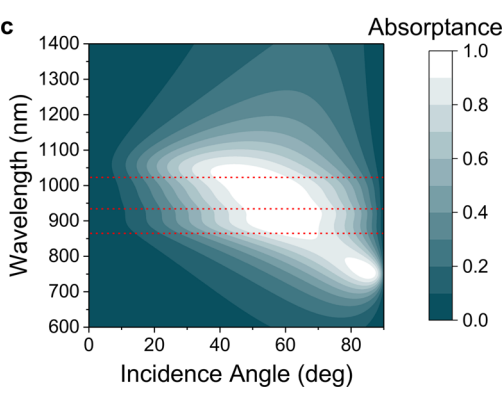


Figure 3. Broadband perfect absorption of three-layer ITO stacks (Figure 1d,e) for the Berreman and ENZ modes. The ITO layers of thicknesses  $t_1$ ,  $t_2$ , and  $t_3$  have electron densities  $N_1 = 1.4 \times 10^{21}$  cm<sup>-3</sup>,  $N_2 = 1.2 \times 10^{21} \text{ cm}^{-3}$ , and  $N_3 = 1.0 \times 10^{21} \text{ cm}^{-3}$ , respectively. (a) Absorptance of the three-layer stacks composed of ITO nanolayers of the same thickness,  $t_1 = t_2 = t_3$  (shaded areas). The total stack thickness is 12 nm for the Berreman mode and 18 nm for the ENZ mode. The solid blue line shows the absorptance of the optimized 3layer stack for the Berreman mode with the total thickness of 19 nm. The incidence angles are 60° (Berreman modes) and 53° (ENZ mode). (b) Thickness optimization of the broadband perfect absorber for the Berreman mode at the incidence angle of 60°. The dots show the PA thicknesses and PA wavelengths of a three-layer perfect absorber with a fixed thickness of  $t_3 = 14$  nm. The three-layer perfect absorber with  $t_3 = 14$  nm and  $t_1 = t_2 = 2.5$  nm has a PA bandwidth of  $50\ nm$  (a thickness plateau in the wavelength range of  $900{-}950\ nm).$ (c) Absorptance of the optimized three-layer ITO stack for the Berreman mode. ITO thicknesses are  $t_3 = 14$  nm and  $t_1 = t_2 = 2.5$  nm. The red dotted lines in (b, c) show the PA wavelengths of 865, 934, and 1023 nm in single ITO layers with the thicknesses  $t_1 = 6.7$  nm,  $t_2 =$ 7.5 nm, and  $t_3 = 8.6$  nm, respectively.

significant increase in the PA bandwidth is achievable through an increase in the number of ITO layers, varying the thickness

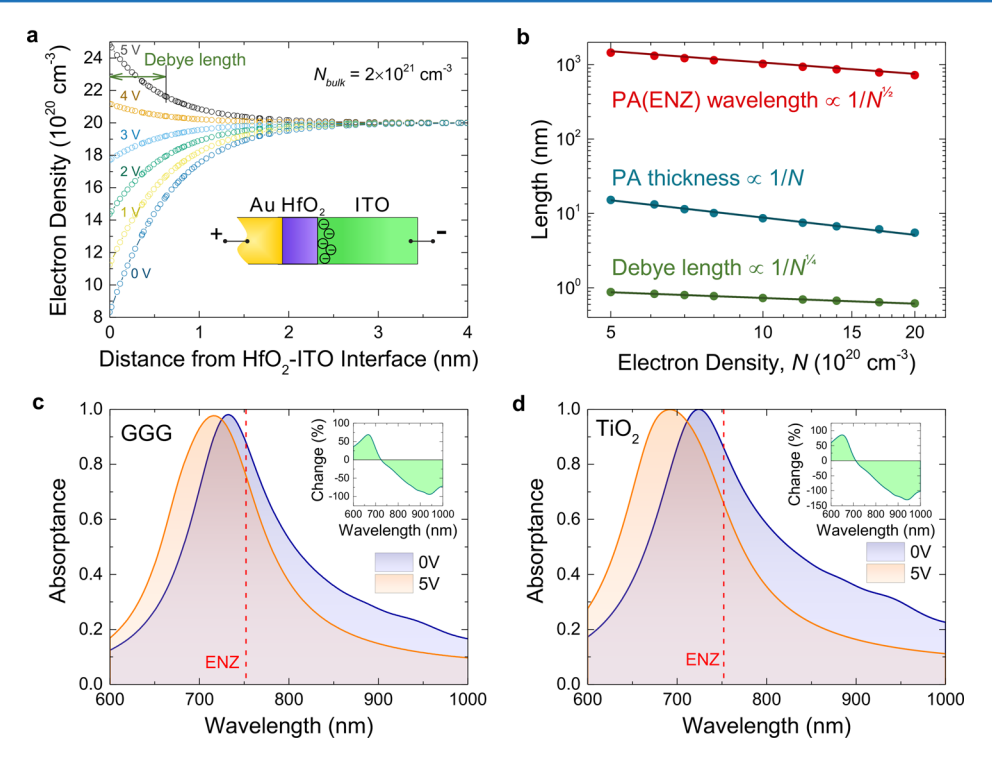


Figure 4. (a) Electron density at the HfO<sub>2</sub>–ITO interface at applied bias of 0–5 V. Inset shows a schematic of the simulated MOS field-effect perfect absorber. The HfO<sub>2</sub> thickness is 5 nm and the bulk electron density of the ITO is  $N=2\times10^{21}$  cm<sup>-3</sup>; (b) Characteristic lengths of the MOS field-effect perfect absorber: PA (ENZ) wavelength, ITO PA thickness at an incidence angle of 60°, and the electron accumulation depth (the Debye length) at 5 V bias. The dots are the numerical results and the lower two lines are linear regressions of  $\propto 1/N^{\alpha}$  ( $\alpha \approx 1$  for the PA thickness and  $\alpha \approx 1/4$  for the Debye length). The ENZ wavelength (red line), calculated from the electron density  $\lambda_{\rm ENZ} \propto 1/N^{1/2}$ , lies slightly above the PA wavelength data (dots). The PA thickness is  $\sim \lambda_{\rm PA}/100$  and decreases faster than either the PA wavelength or the Debye length when electron density increases. (c, d) Perfect absorption tuning: absorptance of the unbiased and 5 V-biased MOS field-effect perfect absorber at the incidence angle of 60°. The ITO bulk electron density is  $2 \times 10^{21}$  cm<sup>-3</sup> and mobility is 31 cm<sup>2</sup>/(V s). The vertical dotted lines show an ENZ wavelength of 752 nm. The insets show the absorptance difference in percent. (c) Incidence medium is GGG and the ITO thickness is 5.5 nm; (d) incidence medium is TiO<sub>2</sub> (rutile) and the ITO thickness is 4 nm. The PA wavelength shifts of 12% and 20% of fwhm and absorptance changes of around 100% are observed under the 5 V bias.

domains of the layers and PA wavelength selection through the manipulation of the carrier densities. Our initial experimental results (Figures S6–S9) show the experimental feasibility of ultrathin single layer and multilayer ENZ selective and broadband perfect absorbers.

In the following section, we discuss a tunable perfect absorber in Berreman configuration with an ITO thickness comparable to the electron accumulation region of the MOS device, utilizing the principles of the multilayer broadband absorber.

Field-Effect Tunable Perfect Absorption. We employ the field-effect tuning of the ENZ frequency of an ITO nanolayer in a MOS-type structure (Figure 1f). <sup>11,12,14</sup> This gate structure allows efficient PA control of the optical confinement based on the accumulated electron distribution and tunable ENZ. This tunable structure is similar to the perfect absorber of Figure 1b, with the addition of 5 nm thick hafnium dioxide (HfO<sub>2</sub>) insulator between metal and the ITO nanolayer. This MOS structure supports the Berreman mode.

The electron density at the interface of the  $HfO_2$  and ITO layers of the MOS absorber is calculated at different bias voltages and various bulk electron densities of the ITO layer (see Methods and Figure S10). An example of the electron density dependence at the  $HfO_2$ –ITO interface on the applied electrical bias between gold and ITO layers is shown in the Figure 4a for the bulk electron density of  $N=2\times10^{21}$  cm<sup>-3</sup>. There is a depletion layer at the interface without bias with a

depth of ~1 nm. As the ITO bulk density increases, the electron density linearly increases at the interface (Figures S10 and S11). As the bias increases, the electron accumulation layer forms and the electron density increases at the interface. The electron density at the interface reaches the value of  $N_i \approx 2.5 \times 10^{21} \, \mathrm{cm}^{-3}$  at a bias of 5 V, that is, the applied electric field of 10 MV/cm. The applied field is below the maximum breakdown field of ultrathin HfO<sub>2</sub> films of 12–16 MV/cm.  $^{37-39}$ 

The depth of the accumulation layer is described by the Debye length  $l_{\rm D} \propto \frac{1}{N_i^{1/2}}$ , where  $N_i$  is the electron density at the HfO<sub>2</sub>–ITO interface. The dependences of the Debye length, the PA wavelength, and PA thickness of the ITO nanolayer on the bulk electron density are shown in Figure 4b. Because the electron density at the interface may be approximated as  $N_i \propto N^{\alpha}$  in the bulk electron density range of  $(5-20) \times 10^{20}$  cm<sup>-3</sup>, where  $\alpha = 0.48 \pm 0.02$  (see Figure S11 for more details), the Debye length  $l_{\rm D} \propto \frac{1}{N^{1/4}}$ . The PA thickness is  $\sim \lambda_{\rm ENZ}/100$  and decreases more rapidly,  $t_{\rm PA} \propto \frac{1}{N}$ , than both the PA wavelength and the Debye length as the electron density increases (Figure 4b). As a result, the PA thickness becomes comparable to the Debye length at high electron densities. This allows the direct tuning of PA in ultrathin ITO films through the application of external electrical bias.

The absorptance and electric field intensity of the MOS perfect absorber are calculated at zero bias and an applied

voltage of 5 V for four different ITO nanolayers (Figures S12-S16) with the bulk electron densities of  $5.0 \times 10^{20}$  cm<sup>-3</sup>,  $6.1 \times$  $10^{20} \text{ cm}^{-3}$ ,  $1.0 \times 10^{21} \text{ cm}^{-3}$ , and  $2.0 \times 10^{21} \text{ cm}^{-3}$ . The ITO thicknesses are 15.2, 13.2, 8.6, and 5.5 nm, respectively, corresponding to the PA condition at an angle of incidence of 60° (Figure 4b). The complex refractive index profiles of the ITO nanolayers in the MOS devices are calculated using the simulated electron density profiles at the HfO2-ITO interface (Figure S10) together with the Drude model. The tunable absorption of the field-effect device is shown in Figure 4c for an ITO nanolayer with a thickness of 5.5 nm and electron density of  $2 \times 10^{21}$  cm<sup>-3</sup>. The shift of the absorptance peak maximum of 16 nm (12% of fwhm) and an absorptance change of around 100% are observed under the applied bias of 5 V. The 98% absorption peaks may be attributed to the depletion/ accumulation layer at the HfO2-ITO interface. To compensate for the depletion/accumulation layer, a thicker ITO layer (6.3 nm) is required to reach PA (Figure S17c). Larger PA shifts could be achieved by increasing the refractive index of the incident medium and increasing electron mobility (decreasing  $Im(\varepsilon_{ITO})$ , see eq 1). Enhanced PA wavelength shifts of ~20% of fwhm and absorptance changes of about 200% are shown in Figures 4d and S17. Increase of the refractive index of the incidence medium (e.g., TiO2 glass, refractive index of 2.5 at 900 nm) and electron mobility (e.g.,  $\mu = 60 \text{ cm}^2/(\text{V} \cdot \text{s})$ ) lead to ITO layers thinner than 5.5 nm (4.0 and 3.7 nm, respectively). Therefore, the PA thickness nears the Debye length (Figure 4b) and stronger impact from the ultrathin accumulation/ depletion layer is expected. It should be noted that the accumulation/depletion layer depends strongly on the material properties such as the Fermi level, energy bandgap, electron affinity, and the dielectric constant of an insulator. Proper selection and optimization of the metal/insulator/semiconductor structures will increase the electron density at the interface and the Debye length (see examples in Figure S18), enhancing the PA tunability. The designed field-effect ENZ structure may be used as an ultrathin (<10 nm) light modulator with the absorption change of ~300% (Figure S19). However, it is beyond the scope of this paper.

## CONCLUSIONS

We show that PA is achievable in ultrathin ENZ layers of  $\sim \lambda_{ENZ}/100$  and discuss the PA thickness dependence on the electron density/ENZ frequency of ITO nanolayers. We present a broadband perfect absorber using multilayered stacks of ultrathin ITO layers with varying electron density. The bandwidth of the perfect absorption is controlled by ENZ wavelengths of individual layers, the number of ENZ layers, and properly designed PA thicknesses. In addition, we illustrate the postfabrication tuning of perfect absorption in ultrathin ITO layers via the field-effect. We show that the PA thickness of the ITO layers is comparable to the Debye length of the electron accumulation layer of the MOS device, leading to an efficient tuning of the perfect absorption by applying electrical bias. The electrical tuning of perfect absorption peak wavelength of about 20% with respect to the fwhm and absorptance changes of more than 200% are demonstrated.

#### METHODS

The absorptance of multilayer films and electric-field intensities as a function of depth in a multilayer stack are calculated by using the IMD software with an algorithm based on recursive

application of the Fresnel equations<sup>40</sup> and by using a MATLAB code developed by G. Figliozzi and F. Michelotti at the University of Rome "La Sapienza" (Italy)<sup>41</sup> based on the transfer matrix method.<sup>42</sup>

A commercial device simulator by Lumerical Solutions, Inc. <sup>43</sup> is used to calculate electron distribution in the MOS device under applied biases. The device simulator uses the finite element method to self-consistently solve the Poisson and drift-diffusion equations. The ohmic contacts at the metal and ITO outer interfaces are set as the boundary conditions. A self-adaptive mesh generation algorithm is used. The maximum refinement steps of 20000 and the minimum mesh size of 5  $\times$  10<sup>-4</sup> nm are used in our simulations. The ITO band structure parameters used in the simulations are energy bandgap of 2.5 eV and electron affinity of 3.5 eV. <sup>44,45</sup> The work function value for gold of 5.1 eV and DC permittivity value of 9.3 for ITO and 25 for HfO<sub>2</sub> are used. <sup>14,46</sup>

## ASSOCIATED CONTENT

# **S** Supporting Information

The Supporting Information is available free of charge on the ACS Publications website at DOI: 10.1021/acsphotonics.7b01373.

Figures S1-S19 (PDF).

#### AUTHOR INFORMATION

#### **Corresponding Authors**

\*E-mail: oleksiy\_anopchenko@baylor.edu.

\*E-mail: howard lee@baylor.edu.

ORCID

Aleksei Anopchenko: 0000-0001-9206-2767

#### **Author Contributions**

H.L. and A.A. conceived the idea. A.A. performed the PA calculations and data analysis. L.T. and A.A. performed calculations of charge distribution in MOS devices. H.L. supervised the project. All authors contributed to the discussion of the results and preparing the manuscript.

#### Notes

The authors declare no competing financial interest.

## ACKNOWLEDGMENTS

This work was supported in part by the Young Faculty Award Program from Defense Advanced Research Projects Agency (Grant Number N66001-17-1-4047), CAREER Award Program from National Science Foundation (Grant Number 1752295), the Young Investigator Development Program, the Undergraduate Research and Scholarly Achievement (URSA), and the Vice Provost for Research at Baylor University. A.A. acknowledges the Office of the Vice Provost for Research at Baylor University for the postdoctoral research fellowship. A.A. thanks Prof. F. Michelotti for the use of the MATLAB code for the transfer matrix calculations.

# REFERENCES

- (1) Kats, M. A.; Capasso, F. Optical absorbers based on strong interference in ultra-thin films. *Laser Photonics Rev.* **2016**, *10*, 735–749. (2) Ra'di, Y.; Simovski, C. R.; Tretyakov, S. A. Thin Perfect Absorbers for Electromagnetic Waves: Theory, Design, and Realizations. *Phys. Rev. Appl.* **2015**, *3*, 037001.
- (3) Ramezani, H.; Wang, Y.; Yablonovitch, E.; Zhang, X. Unidirectional Perfect Absorber. *IEEE J. Sel. Top. Quantum Electron.* **2016**, 22, 115–120.

- (4) Sturmberg, B. C. P.; Chong, T. K.; Choi, D.-Y.; White, T. P.; Botten, L. C.; Dossou, K. B.; Poulton, C. G.; Catchpole, K. R.; McPhedran, R. C.; Martijn de Sterke, C. Total absorption of visible light in ultrathin weakly absorbing semiconductor gratings. *Optica* **2016**, *3*, 556–562.
- (5) Nefedov, I. S.; Valagiannopoulos, C. A.; Melnikov, L. A. Perfect absorption in graphene multilayers. *J. Opt.* **2013**, *15*, 114003.
- (6) Chang, Y. C.; Kildishev, A. V.; Narimanov, E. E.; Norris, T. B. Metasurface perfect absorber based on guided resonance of a photonic hypercrystal. *Phys. Rev. B: Condens. Matter Mater. Phys.* **2016**, *94*, 155430.
- (7) Lee, Y. P.; Rhee, J. Y.; Yoo, Y. J.; Kim, K. W. Metamaterials for Perfect Absorption; Springer: Singapore, 2016.
- (8) Zheludev, N. I.; Kivshar, Y. S. From metamaterials to metadevices. *Nat. Mater.* **2012**, *11*, 917–924.
- (9) Kats, M. A.; Sharma, D.; Lin, J.; Genevet, P.; Blanchard, R.; Yang, Z.; Qazilbash, M. M.; Basov, D. N.; Ramanathan, S.; Capasso, F. Ultrathin perfect absorber employing a tunable phase change material. *Appl. Phys. Lett.* **2012**, *101*, 221101.
- (10) Lee, J.; Jung, S.; Chen, P.-Y.; Lu, F.; Demmerle, F.; Boehm, G.; Amann, M.-C.; Alù, A.; Belkin, M. A. Ultrafast Electrically Tunable Polaritonic Metasurfaces. *Adv. Opt. Mater.* **2014**, *2*, 1057–1063.
- (11) Park, J.; Kang, J. H.; Liu, X. G.; Brongersma, M. L. Electrically Tunable Epsilon-Near-Zero (ENZ) Metafilm Absorbers. *Sci. Rep.* **2015**, *5*, 15754.
- (12) Shi, K. F.; Lu, Z. L. Field-effect optical modulation based on epsilon-near-zero conductive oxide. *Opt. Commun.* **2016**, *370*, 22–28.
- (13) Li, Z.; Zhou, Y.; Qi, H.; Pan, Q.; Zhang, Z.; Shi, N. N.; Lu, M.; Stein, A.; Li, C. Y.; Ramanathan, S.; Yu, N. Correlated Perovskites as a New Platform for Super-Broadband-Tunable Photonics. *Adv. Mater.* **2016**, 28, 9117–9125.
- (14) Huang, Y. W.; Lee, H. W. H.; Sokhoyan, R.; Pala, R. A.; Thyagarajan, K.; Han, S.; Tsai, D. P.; Atwater, H. A. Gate-Tunable Conducting Oxide Metasurfaces. *Nano Lett.* **2016**, *16*, 5319–5325.
- (15) Arroyo Huidobro, P.; Maier, S. A.; Pendry, J. B. Tunable plasmonic metasurface for perfect absorption. *EPJ. Appl. Metamat.* **2017**, *4*, 6.
- (16) Vassant, S.; Archambault, A.; Marquier, F.; Pardo, F.; Gennser, U.; Cavanna, A.; Pelouard, J. L.; Greffet, J. J. Epsilon-Near-Zero Mode for Active Optoelectronic Devices. *Phys. Rev. Lett.* **2012**, *109*, 237401.
- (17) Yoon, J.; Zhou, M.; Badsha, M. A.; Kim, T. Y.; Jun, Y. C.; Hwangbo, C. K. Broadband Epsilon-Near-Zero Perfect Absorption in the Near-Infrared. *Sci. Rep.* **2015**, *5*, 12788.
- (18) Newman, W. D.; Cortes, C. L.; Atkinson, J.; Pramanik, S.; DeCorby, R. G.; Jacob, Z. Ferrell-Berreman Modes in Plasmonic Epsilon-near-Zero Media. *ACS Photonics* **2015**, *2*, 2–7.
- (19) Campione, S.; Kim, I.; de Ceglia, D.; Keeler, G. A.; Luk, T. S. Experimental verification of epsilon-near-zero plasmon polariton modes in degenerately doped semiconductor nanolayers. *Opt. Express* **2016**, *24*, 18782–18789.
- (20) Berreman, D. W. Infrared absorption at longitudinal optic frequency in cubic crystal films. *Phys. Rev.* **1963**, *130*, 2193–2198.
- (21) Vassant, S.; Hugonin, J.-P.; Marquier, F.; Greffet, J.-J. Berreman mode and epsilon near zero mode. *Opt. Express* **2012**, *20*, 23971–23977.
- (22) Luk, T. S.; Campione, S.; Kim, I.; Feng, S. M.; Jun, Y. C.; Liu, S.; Wright, J. B.; Brener, I.; Catrysse, P. B.; Fan, S. H.; Sinclair, M. B. Directional perfect absorption using deep subwavelength low-permittivity films. *Phys. Rev. B: Condens. Matter Mater. Phys.* **2014**, 90, 085411.
- (23) Badsha, M. A.; Jun, Y. C.; Hwangbo, C. K. Admittance matching analysis of perfect absorption in unpatterned thin films. *Opt. Commun.* **2014**, 332, 206–213.
- (24) Campione, S.; Brener, I.; Marquier, F. Theory of epsilon-near-zero modes in ultrathin films. *Phys. Rev. B: Condens. Matter Mater. Phys.* **2015**, *91*, 121408.
- (25) Lee, H. W.; Papadakis, G.; Burgos, S. P.; Chander, K.; Kriesch, A.; Pala, R.; Peschel, U.; Atwater, H. A. Nanoscale Conducting Oxide PlasMOStor. *Nano Lett.* **2014**, *14*, 6463–6468.

(26) Li, H.; Xu, S.; Wang, H.; Gu, Y.; Lombardi, J. R.; Xu, W. Active-Tuned Plasmonic Angle Modulator of Light Beams for Potential Application of 3D Display. *ACS Photonics* **2014**, *1*, 677–682.

- (27) Babicheva, V. E.; Lavrinenko, A. V. Plasmonic modulator optimized by patterning of active layer and tuning permittivity. *Opt. Commun.* **2012**, *285*, 5500–5507.
- (28) Shi, K. F.; Haque, R. R.; Zhao, W. S.; Zhao, R. C.; Lu, Z. L. Tunable plasmonic metamaterial based on transparent conducting oxide. *Proc. SPIE* **2014**, *8980*, *898012*.
- (29) Raether, H. Surface plasmons on smooth and rough surfaces and on gratings. Springer, 1988.
- (30) Wood, D. L.; Nassau, K. Optical properties of gadolinium gallium garnet. *Appl. Opt.* **1990**, *29*, 3704–3707.
- (31) Olmon, R. L.; Slovick, B.; Johnson, T. W.; Shelton, D.; Oh, S. H.; Boreman, G. D.; Raschke, M. B. Optical dielectric function of gold. *Phys. Rev. B: Condens. Matter Mater. Phys.* **2012**, *86*, 235147.
- (32) Holman, Z. C.; Filipic, M.; Descoeudres, A.; De Wolf, S.; Smole, F.; Topic, M.; Ballif, C. Infrared light management in high-efficiency silicon heterojunction and rear-passivated solar cells. *J. Appl. Phys.* **2013**, *113*, 013107.
- (33) Kim, H.; Gilmore, C. M.; Pique, A.; Horwitz, J. S.; Mattoussi, H.; Murata, H.; Kafafi, Z. H.; Chrisey, D. B. Electrical, optical, and structural properties of indium-tin-oxide thin films for organic light-emitting devices. *J. Appl. Phys.* **1999**, *86*, 6451–6461.
- (34) Tuna, O.; Selamet, Y.; Aygun, G.; Ozyuzer, L. High quality ITO thin films grown by dc and RF sputtering without oxygen. *J. Phys. D: Appl. Phys.* **2010**, *43*, 055402.
- (35) Shah, D.; Reddy, H.; Kinsey, N.; Shalaev, V. M.; Boltasseva, A. Optical Properties of Plasmonic Ultrathin TiN Films. *Adv. Opt. Mater.* **2017**, *5*, 1700065.
- (36) Anopchenko, A.; Lee, H. W. H. ENZ; Conducting Oxide Broadband Perfect Absorbers with Deep Sub-Wavelength Thicknesses. In *Conference on Lasers and Electro-Optics*, San Jose, California, 2017/05/14; Optical Society of America: San Jose, CA, 2017; p JTh2A.94.
- (37) Kang, L.; Lee, B. H.; Qi, W. J.; Jeon, Y.; Nieh, R.; Gopalan, S.; Onishi, K.; Lee, J. C. Electrical characteristics of highly reliable ultrathin hafnium oxide gate dielectric. *IEEE Electron Device Lett.* **2000**, 21, 181–183.
- (38) Vasil'ev, A. G.; Zakharov, R. A.; Orlikovskii, A. A.; Rogozhin, A. E.; Sonin, M. S.; Khorin, I. A. Electrophysical characteristics of HfO<sub>2</sub> gate structures formed by electron-beam evaporation. *Philometric Philometric Philometri*
- (39) Sire, C.; Blonkowski, S.; Gordon, M. J.; Baron, T. Statistics of electrical breakdown field in HfO<sub>2</sub> and SiO<sub>2</sub> films from millimeter to nanometer length scalesStatistics of electrical breakdown field in HfO<sub>2</sub> and SiO<sub>2</sub> films from millimeter to nanometer length scales. *Appl. Phys. Lett.* **2007**, *91*, 242905.
- (40) Windt, D. L. IMD Software for modeling the optical properties of multilayer films. *Comput. Phys.* **1998**, *12*, 360–370.
- (41) Anopchenko, A.; Occhicone, A.; Rizzo, R.; Sinibaldi, A.; Figliozzi, G.; Danz, N.; Munzert, P.; Michelotti, F. Effect of thickness disorder on the performance of photonic crystal surface wave sensors. *Opt. Express* **2016**, *24*, 7728–7742.
- (42) Yeh, P.; Yariv, A.; Hong, C.-S. Electromagnetic propagation in periodic stratified media. I. General theory. *J. Opt. Soc. Am.* **1977**, *67*, 423–438.
- (43) Lumerical Solutions, Inc. http://www.lumerical.com/tcad-products/device.
- (44) Klein, A. Electronic properties of In2O3 surfaces. *Appl. Phys. Lett.* **2000**, *77*, 2009–2011.
- (45) Korber, C.; Krishnakumar, V.; Klein, A.; Panaccione, G.; Torelli, P.; Walsh, A.; Da Silva, J. L. F.; Wei, S. H.; Egdell, R. G.; Payne, D. J. Electronic structure of In<sub>2</sub>O<sub>3</sub> and Sn-doped In<sub>2</sub>O<sub>3</sub> by hard x-ray photoemission spectroscopy. *Phys. Rev. B: Condens. Matter Mater. Phys.* **2010**, *81*, 165207.
- (46) Wilk, G. D.; Wallace, R. M.; Anthony, J. M. High-kappa gate dielectrics: Current status and materials properties considerations. *J. Appl. Phys.* **2001**, *89*, 5243–5275.